Parity-time–symmetry breaking in two-dimensional photonic crystals: Square lattice

Adam Mock[*]

School of Engineering and Technology, Central Michigan University, Mount Pleasant, Michigan 48859, USA
and Science of Advanced Materials Program, Central Michigan University, Mount Pleasant, Michigan 48859, USA
(Received 25 February 2016; published 9 June 2016)

We consider theoretically materials whose electromagnetic properties possess parity-time ($\mathcal{PT}$) symmetry and are periodic in two dimensions. When designed for optical frequencies such structures are commonly known as two-dimensional (2D) photonic crystals. With the addition of $\mathcal{PT}$ symmetry the optical modes of 2D photonic crystals exhibit thresholdless spontaneous $\mathcal{PT}$-symmetry breaking near the Brillouin zone boundary, which is analogous to what has previously been studied in $\mathcal{PT}$-symmetric structures with one-dimensional periodicity. Consistent with previous work, we find that spontaneous $\mathcal{PT}$-symmetry breaking occurs at band crossings in the photonic dispersion diagram. Due to the extra spatial degree of freedom in 2D periodic systems, their band structures contain more band crossings and higher-order degeneracies than their one-dimensional counterparts. This work provides a comprehensive theoretical analysis of spontaneous $\mathcal{PT}$-symmetry breaking at these points in the band structure. We find that, as in the case of one-dimensional structures, photonic band gaps exist at $k = 0$. We also find that at points of degeneracy with order higher than 2, bands merge pairwise to form broken-$\mathcal{PT}$-symmetry supermodes. If the degeneracy order is even, this means multiple pairs of bands can form distinct (nondegenerate) broken-symmetry supermodes. If the order of degeneracy is odd, at least one of the bands will have protected $\mathcal{PT}$ symmetry. At other points of degeneracy, we find that the $\mathcal{PT}$ symmetry of the modes may be protected and we provide a spatial mode symmetry argument to explain this behavior. Finally, we identify a point at which two broken-$\mathcal{PT}$-symmetry supermodes become degenerate, creating a point of fourfold degeneracy in the broken-$\mathcal{PT}$-symmetry regime.

I. INTRODUCTION

Since the discovery that quantum systems invariant under a combined parity $\mathcal{P}$ and time-reversal $\mathcal{T}$ operation have real eigenvalues [1–3], a variety of theoretical and experimental studies of such systems have appeared in the literature. Because of the duality of the electromagnetic wave equation with the stationary Schrödinger equation and the mature state of photonic materials processing, many of the experimental studies of systems possessing $\mathcal{PT}$ symmetry have been electromagnetic in nature [4–9]. One of the most fascinating aspects of $\mathcal{PT}$-symmetric systems is the observation of spontaneous $\mathcal{PT}$-symmetry breaking. $\mathcal{PT}$ symmetry is broken when the magnitude of the balanced gain and loss is increased and two nominally real eigenvalues merge into a complex-conjugate pair. The point on a phase diagram at which this merging occurs is known as an exceptional point [10]. Intuitively, the exceptional point occurs when the magnitude of the rate of gain or loss is increased past the coupling rate between the gain and loss regions of the system.

The structures studied in the majority of previous reports of electromagnetic systems with $\mathcal{PT}$ symmetry possess this symmetry along only one spatial direction. For example, lossless propagation and $\mathcal{PT}$-symmetry breaking have been demonstrated in two coupled waveguides where one guide is amplifying and the other is dissipative at a rate equal but opposite in sign to the amplifying guide [11–13]. In this case the single $\mathcal{PT}$-symmetry plane is parallel to the waveguides but perpendicular to the plane of the guides and located at the midpoint between them. Several groups

have exploited $\mathcal{PT}$ symmetry and $\mathcal{PT}$-symmetry breaking for device applications using microring resonators [14–19]. Previous reports have also studied metamaterials possessing $\mathcal{PT}$ symmetry [20–22] where the gain and loss and their associated spectral dependence provide another avenue for engineering the optical properties of the material while also providing theoretically lossless propagation.

A number of previous works have studied structures with periodic $\mathcal{PT}$ symmetry. The majority of these studies have dealt with periodicity in only one dimension [23–30]. To date, there have been few investigations into the properties of systems possessing $\mathcal{PT}$ symmetry in dimensions higher than one. Makris *et al.* and Regensburger *et al.* have studied $\mathcal{PT}$-symmetric mesh-periodic networks in a fiber and 50:50 fiber coupler platform [31–33]. Agarwal *et al.* explored $\mathcal{PT}$-symmetry breaking in exactly solvable two-dimensional (2D) problems [34]. Ge and Stone proved general conditions for thresholdless $\mathcal{PT}$-symmetry breaking in 2D disks and three-dimensional spheres [35]. Ge *et al.* studied general properties of multimode waveguides possessing $\mathcal{PT}$ symmetry [36]. Xie *et al.* and Wang *et al.* have studied soliton formation in nonlinear materials with a 2D sinusoidal modulation of the loss and gain [37,38]. While these studies have touched on various aspects of 2D $\mathcal{PT}$-symmetric structures, studies of the fundamental behavior of 2D periodic electromagnetic systems possessing $\mathcal{PT}$ symmetry are lacking.

In the present work we conduct a comprehensive theoretical analysis of structures possessing periodic $\mathcal{PT}$ symmetry in two dimensions. Here we refer to such a structure as a 2D $\mathcal{PT}$-symmetric photonic crystal (PC). An example of such a structure is depicted in Fig. 1. In this case the 2D $\mathcal{PT}$ symmetric PC is a square lattice whose basis consists of two vertically oriented rods with circular cross section.
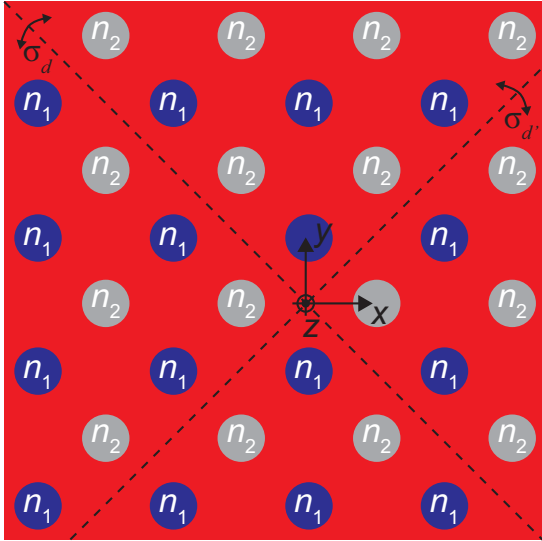
———————
[*]mock1ap@cmich.edu

FIG. 1. Schematic diagram showing the two-dimensional $\mathcal{PT}$-symmetric photonic crystal. Rods labeled n_1 are the gain rods ($n_1 = n_r + in_i$) and rods labeled n_2 are the loss rods ($n_2 = n_r - in_i$) for positive n_r and n_i. The structure possesses $\mathcal{PT}$ symmetry if the parity operation is defined by the reflection σ_d or $\sigma_{d'}$.

The background refractive index is n_r. The rods labeled n_1 are amplifying (gain rods) and have a complex refractive index given by $n_1 = n_r + in_i$ for positive n_r and n_i and the rods labeled n_2 are absorbing (loss rods) with a complex refractive index given by $n_2 = n_r - in_i$. We note that in this study we consider geometries in which the real part of the refractive index is uniform. The 2D $\mathcal{PT}$-symmetric PC is defined strictly by the imaginary part of the refractive index. Figure 1 depicts two $\mathcal{PT}$-symmetry planes labeled by σ_d and $\sigma_{d'}$. Conventionally the symbol σ is reserved for the reflection or $\mathcal{P}$ operation. The 2D $\mathcal{PT}$-symmetric PC is not invariant under σ_d or $\sigma_{d'}$ alone. However, with the additional operation of $\mathcal{T}$ that becomes a complex conjugation in the frequency domain, the structure is indeed invariant.

We begin the analysis by obtaining exactly solvable results for a 1D $\mathcal{PT}$-symmetric periodic structure. We use these analytical results to explain various features of the structure's photonic band structure. We then show that many of these properties are retained in the 2D $\mathcal{PT}$-symmetric PC. Further, the 2D $\mathcal{PT}$-symmetric PC band diagram contains a variety of behavior not seen in the 1D case and we explore these behaviors in detail. As pointed out by Ge and Stone, a necessary condition for $\mathcal{PT}$-symmetry breaking is degeneracy in the eigenvalues when the gain and loss magnitude is zero [35]. In a 2D PC, degeneracy occurs at band crossings. These usually occur at high-symmetry points at the Brillouin zone boundary. However, they also appear at low-symmetry points within the Brillouin zone due to multidirectional band folding [39] and we describe the $\mathcal{PT}$ symmetry of the modes at these crossings. A particularly interesting discovery is the identification of band crossings in which $\mathcal{PT}$ symmetry is *protected* and we provide a spatial-field symmetry argument to explain this behavior. We also find that at band crossings involving more than two bands, $\mathcal{PT}$-symmetry breaking is manifested by pairwise band merging. When the band crossing

involves an odd number of bands, the pairwise criterion still holds and the $\mathcal{PT}$ symmetry of the remainder band is protected.

II. EXACTLY SOLVABLE MODEL: ONE-DIMENSIONAL PERIODIC STRUCTURES WITH $\mathcal{PT}$ SYMMETRY

Figure 2(a) depicts a 1D periodic structure with $\mathcal{PT}$ symmetry. Each layer has thickness L and the refractive indices are complex and conjugate to each other $n_1 = n_r + in_i$ and $n_2 = n_r - in_i$. The $\mathcal{PT}$-symmetry planes occur at the interfaces between any of the layers. In this study the real part will be set to $n_r = 2.0$ while the imaginary part will take on values between 0 and 0.2. These values are chosen to illustrate the concepts of $\mathcal{PT}$ symmetry in periodic structures simply and effectively while still being roughly consistent with typical solid-state materials at optical frequencies. We acknowledge that a gain coefficient corresponding to $n_i = 0.2$ would be about a factor of 5 larger than what is typically available in semiconductor gain materials [40], but we proceed with this number in the present work for purposes of illustration. Also, we note briefly that the gain-loss pattern described in Fig. 1 could be experimentally realized in semiconductor gain
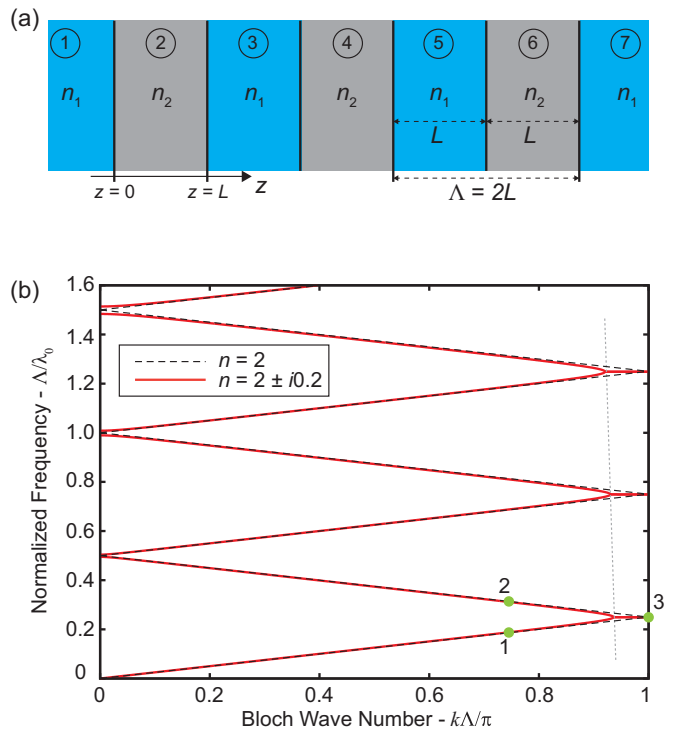

FIG. 2. (a) Schematic diagram showing a one-dimensional periodic $\mathcal{PT}$-symmetric structure. Layers labeled n_1 are the gain layers ($n_1 = n_r + in_i$) and layers labeled n_2 are the loss layers ($n_2 = n_r - in_i$) for positive n_r and n_i. Each layer has a thickness L and the period of the periodic structure is $\Lambda = 2L$. (b) Photonic band diagram for propagation through the structure in (a). Bands for $n_i = 0$ (black dashed line) and $n_i = 0.2$ (red solid line) are shown. The light gray fine dashed line shows the exceptional point for various bands with $n_i = 0.2$. The green dots correspond to the fields shown in Fig. 4.

material with a spatially selective passivation technique [41] or through masked regrowth [42].

To obtain analytical results we use the propagation matrix method [43]. The electric field for normal incidence on a 1D layered structure is given by forward and backward propagating transverse electromagnetic plane waves. In layer q, the electric field is given by

$$E_q(z) = E_q^+ \exp(-ik_q z) + E_q^- \exp(ik_q z), \tag{1}$$

where $E_q(z)$ represents a transverse component of the electric field and $k_q = k_0 n_q$, where k_0 is the vacuum wave number. The amplitudes E_q^+ and E_q^- correspond to the field at the inner side of the rightmost boundary of the qth layer. For example, for layer $q = 1$ in Fig. 2(a), $E_1(0^-) = E_1^+ + E_1^-$, where 0^- represents the layer 1 side of the $z = 0$ boundary. The fields in the adjacent layer $q = 2$ can be related to those in layer $q = 1$ by a 2×2 propagation matrix $\boldsymbol{P}_{1,2}$. The elements in $\boldsymbol{P}_{1,2}$ result from enforcing boundary conditions on E_1, H_1 and E_2, H_2 at the boundary between layers 1 and 2 and propagating the fields through layer 2. The ensuing field amplitudes E_2, H_2 apply to the inner side of the rightmost boundary of the $q = 2$ layer. Generally, for propagation from layer q to layer $q + 1$ one has

$$\boldsymbol{P}_{q,q+1} \begin{bmatrix} E_q^+ \\ E_q^- \end{bmatrix} = \begin{bmatrix} E_{q+1}^+ \\ E_{q+1}^- \end{bmatrix}, \tag{2}$$

where the right-hand side represents the field amplitudes at the inner side of the rightmost boundary of the $q + 1$ layer.

If the 1D layered structure consists of equal length layers with alternating refractive indices as indicated in Fig. 2(a), then propagation through two adjacent layers constitutes traversing one period of the periodic structure. In this case, Bloch's theorem as applied to electromagnetic waves [44] may be invoked to write

$$\boldsymbol{P}_{q,q+2} \begin{bmatrix} E_q^+ \\ E_q^- \end{bmatrix} = \begin{bmatrix} E_{q+2}^+ \\ E_{q+2}^- \end{bmatrix} = e^{-ik\Lambda} \begin{bmatrix} E_q^+ \\ E_q^- \end{bmatrix}. \tag{3}$$

Therefore, the eigenvalues of the two-layer propagation matrix $\boldsymbol{P}_{q,q+2}$ have the form $\exp(-ik\Lambda)$. Let the components of $\boldsymbol{P}_{q,q+2}$ be labeled as

$$\boldsymbol{P}_{q,q+2} = \begin{bmatrix} p_{11} & p_{12} \\ p_{21} & p_{22} \end{bmatrix}. \tag{4}$$

For the case shown in Fig. 2(a) we obtain

$$p_{11} = \frac{e^{-jk_0 n_2 L}}{n_r^2 + n_i^2} \left[n_r^2 e^{-jk_0 n_1 L} + n_i^2 e^{jk_0 n_1 L} \right], \tag{5}$$

$$p_{12} = \frac{2 n_r n_i e^{-jk_0 n_2 L}}{n_r^2 + n_i^2} \sin(k_0 n_1 L), \tag{6}$$

$$p_{21} = -\frac{2 n_r n_i e^{jk_0 n_2 L}}{n_r^2 + n_i^2} \sin(k_0 n_1 L), \tag{7}$$

$$p_{22} = \frac{e^{jk_0 n_2 L}}{n_r^2 + n_i^2} \left[n_r^2 e^{jk_0 n_1 L} + n_i^2 e^{-jk_0 n_1 L} \right]. \tag{8}$$

Because $\boldsymbol{P}_{q,q+2}$ is unimodular $(p_{11}p_{22} - p_{12}p_{21} = 1)$, its eigenvalues are given by

$$e^{-jk\Lambda} = \tfrac{1}{2} [p_{11} + p_{22} \pm \sqrt{(p_{11} + p_{22})^2 - 4}]. \tag{9}$$

The quantity $p_{11} + p_{22}$ can be simplified to

$$p_{11} + p_{22} = 2 \frac{n_r^2 \cos(2k_0 n_r L) + n_i^2 \cosh(2k_0 n_i L)}{n_r^2 + n_i^2}. \tag{10}$$

Now we consider a few points of interest. First consider the Bragg wavelength $\lambda_0 = 2(n_1 L + n_2 L) = 4n_r L$:

$$[p_{11} + p_{22}]_{\lambda_0} = 2 \frac{-n_r^2 + n_i^2 \cosh(\pi n_i / n_r)}{n_r^2 + n_i^2}. \tag{11}$$

For small values of n_i such that $\pi n_i / n_r \ll 1$,

$$[p_{11} + p_{22}]_{\lambda_0} \approx -2 \frac{n_r^2 - n_i^2}{n_r^2 + n_i^2}. \tag{12}$$

From this one concludes that the quantity under the radical in Eq. (9) is negative. Equating real parts of Eq. (9) yields

$$\cos(k\Lambda) \approx -\frac{n_r^2 - n_i^2}{n_r^2 + n_i^2} > -1, \tag{13}$$

so at the Bragg wavelength $k < \pi/\Lambda$ and the dispersion curve does not reach the Brillouin zone boundary $k = \pi/\Lambda$ for real frequencies (i.e., real k_0). Furthermore, because the Bloch wave number k remains purely real at this point, Bragg reflection is not expected in this frequency region. Figure 2(b) shows the photonic band diagram for this 1D periodic structure. The band structure was calculated using the plane-wave expansion method [45]. In principle, the propagation matrix method can be used, but because it uses frequency as an input parameter and determines the Bloch wave vector k, the input parameter space is two dimensional (real and imaginary parts of frequency), which complicates the calculation. The plane-wave expansion method uses k as a parameter and determines frequencies, which can be complex in general.

Upon close inspection of Fig. 2(b) one can see the presence of exceptional points near $k\Lambda/\pi = 1$. At these points, adjacent bands merge and become degenerate in their real frequency, while their complex components become nonzero and complex conjugate to each other. The transition from real to complex-conjugate frequency eigenvalues is the hallmark of spontaneous $\mathcal{PT}$-symmetry breaking. Figure 3(a) shows a close-up of the region near $k\Lambda/\pi = 1$ for several values of n_i. The critical point moves to lower k values with increasing n_i consistent with Eq. (13). We note also that $k < \pi/\Lambda$ for *any* nonzero n_i, which indicates that this $\mathcal{PT}$-symmetry breaking is thresholdless. Figure 3(b) shows the imaginary part of the frequency as a function of k. The imaginary part is zero for k values to the left of the critical point. At the critical point, the two merged bands have nonzero imaginary parts that are negatives of each other. The imaginary part increases monotonically with k from the critical point to the Brillouin zone boundary.

We also point out that for higher-order bands, the critical point moves slightly to the left. This can be predicted analytically by keeping a higher-order term in the approximation for $\cosh(2k_0 n_i L)$ in Eq. (11). The trend is depicted by the fine dashed line in Fig. 2(b).

Close inspection of Fig. 2(b) reveals that photonic band gaps exist near band crossings at $k = 0$ similar to those of
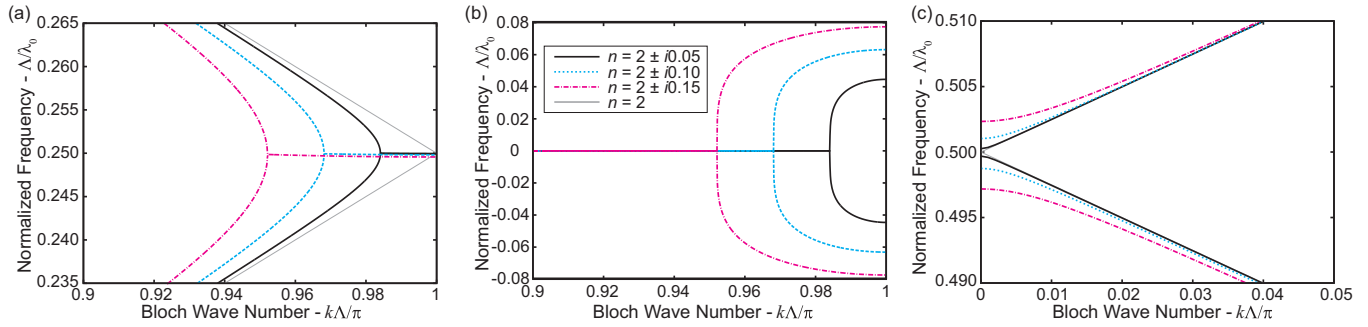
FIG. 3. (a) Zoomed-in version of Fig. 2(b) at the lowest-frequency exceptional point. Included here are curves corresponding to $n_i = 0.05$, 0.10, and 0.15. (b) Imaginary part of the frequencies for the bands shown in (a). The frequencies of the broken-$\mathcal{PT}$-symmetry bands are complex conjugate to each other. (c) Zoomed-in version of the band behavior at $k = 0$. Instead of spontaneous $\mathcal{PT}$-symmetry breaking, a photonic band gap exists whose width grows with increasing n_i.

lossless 1D gratings. Performing a similar analysis as above on the propagation matrix at $\lambda_0 = n_1 L + n_2 L = 2n_r L$ yields

$$p_{11} + p_{22} = 2\frac{n_r^2 + n_i^2 \cosh(2\pi n_i/n_r)}{n_r^2 + n_i^2}. \quad (14)$$

This result shows that $p_{11} + p_{22} > 2$, which results in a real value on the right-hand side of Eq. (9). However, this real value is greater than one, so the resulting k is complex and this is the usual criterion for a photonic band gap [43]. Based on this analysis, one does not anticipate exceptional point behavior near $k = 0$. Figure 3(c) shows the evolution of the bands near $k = 0$ for increasing values of n_i. The band-gap size increases with increasing n_i.

Figure 4 depicts the spatial field distribution associated with two k points in the band diagram. Figure 4(a) depicts the field at points 1 and 2 in Fig. 2(b), which is in the $\mathcal{PT}$-symmetry region. The magenta dashed line is associated with point 1 and the purple solid line is associated with point 2. In this case the mode frequencies are real. Inspection of the fields shows the usual first-order (point 1) and second-order (point 2) band behavior. However, in both cases the fields overlap the gain (labeled G with refractive index n_1) and absorbing

(labeled A with refractive index n_2) regions equally, resulting in a net gain-loss balance and real frequency eigenvalue. In the broken-$\mathcal{PT}$-symmetry region, the modes hybridize and overlap the gain and absorption regions differently. Figure 4(b) shows the mode fields at $k\Lambda/\pi = 1$, which is in the broken-$\mathcal{PT}$-symmetry regime. The fields for the two bands exhibit similar spatial dependence, but one field is localized in the gain regions and the other is localized in the absorption regions. In this case the fields for the two modes exhibit the same spatial behavior aside from a shift of $\Lambda/2$ along the z direction.

We note that the band diagrams shown here for the 1D $\mathcal{PT}$-symmetric lattices bear some resemblance to those of 1D lattices with layers of alternating positive and negative *real* parts of the index [46]. In particular, the 1D periodic structures with positive and negative real refractive indices have band diagrams with gaps at $k = 0$ and dispersion curves whose real part truncates before the Brillouin zone boundary. Similar results were found for a nominally lossless 1D periodic quarter-wave stack that incorporated graphene monolayers at the interfaces between the low and high index layers [47]. However, in these cases, exceptional point behavior associated with $\mathcal{PT}$-symmetry breaking does not occur.
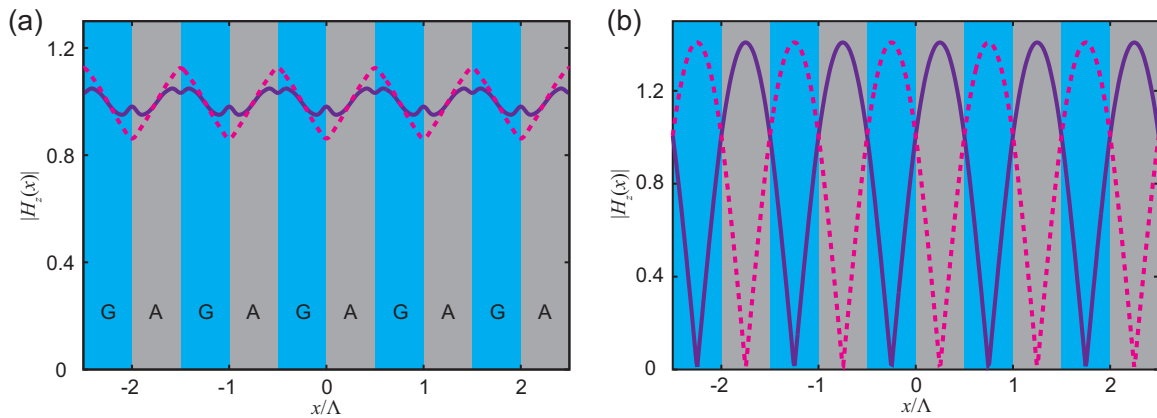

FIG. 4. Depiction of the field in the 1D periodic structure with $\mathcal{PT}$ symmetry. G labels the gain layers (n_1) and A labels the absorbing layers (n_2). The two curves in (a) correspond to points 1 and 2 in Fig. 2(b) (magenta dashed line, point 1; purple solid line, point 2). These modes are in the $\mathcal{PT}$-symmetry regime with equal overlap with the gain and absorbing layers. (b) Fields corresponding to point 3 in Fig. 2(b). These fields are in the broken-$\mathcal{PT}$-symmetry regime with preferential overlap of the gain layers (gain mode, magenta dashed line) or the absorption layers (loss mode, purple solid line).

III. TWO-DIMENSIONAL PERIODIC STRUCTURES WITH $\mathcal{PT}$ SYMMETRY

Here we extend the analysis of periodic structures with $\mathcal{PT}$ symmetry to two dimensions. In the previous section we determined that points of interest on the photonic band structure fell into two classes: (a) regions near the Brillouin zone boundary in which thresholdless $\mathcal{PT}$-symmetry breaking occurs and (b) regions at $k=0$ in which $\mathcal{PT}$-symmetry breaking does not occur, but rather a photonic band gap exists instead. In the following we will show that these two types of points also occur for 2D $\mathcal{PT}$-symmetric photonic crystals. However, in the 2D case a rich variety of additional behavior is observed. These behaviors include $\mathcal{PT}$-symmetry breaking at midzone band crossings, protected $\mathcal{PT}$ symmetry at certain band crossings, and $\mathcal{PT}$-symmetry breaking behavior at points of degeneracy with order greater than 2.

Figure 1 shows the geometry of the structure. It is a 2D square lattice with a unit cell consisting of two circular rods. The gain rod has $n_1 = n_r + in_i$ and the loss rod has $n_2 = n_r - in_i$. The background refractive index is set to n_r (i.e., the real part of the refractive index is uniform throughout the structure). The results reported here use $n_r = 2.0$ and $n_i = 0.25$. The rods have a radius of $r = 0.2\Lambda$, where Λ is the spatial period. The dashed lines in Fig. 1 indicate the reflection planes for the parity operation such that $\mathcal{PT}n(x,y) = \sigma_d \mathcal{T}n(x,y) = \sigma_d n^*(x,y) = n^*(y,x) = n(x,y)$ and $\mathcal{PT}n(x,y) = \sigma_{d'} \mathcal{T}n(x,y) = \sigma_{d'}n^*(x,y) = n^*(-y,-x) = n(x,y)$, where it is noted that the $\mathcal{T}$ operation is a complex conjugation in the phasor domain.

Figure 5 shows the band structure of the 2D $\mathcal{PT}$-symmetric PC shown in Fig. 1 calculated using the plane-wave expansion method [45]. In the results that follow, the electric field is polarized in the x-y plane and the only nonzero magnetic field component is $H_z(x,y)$. We reserve the complementary polarization (H_x, H_y, E_z) for a future study. Figure 5(a) shows the photonic band structure for a material of index $n_r = 2$ with an infinitesimally small square lattice perturbation. Essentially, it shows the light line in the uniform material folded into what would be the first Brillouin zone for a 2D square lattice. This diagram shows the nominal band crossings and band degeneracies. As the imaginary part of the refractive index is increased gradually from zero, $\mathcal{PT}$-symmetry-breaking behavior will be seen most obviously at band crossings and in degenerate bands. Figure 5(b) shows the photonic band structure in which $n_1 = 2.0 + i0.25$ and $n_2 = 2.0 - i0.25$. Figure 5(c) shows the imaginary frequencies for the bands in Fig. 5(b). As expected, Figs. 5(a) and 5(b) look similar. However, closer inspection shows that previously degenerate bands are nondegenerate in the $\mathcal{PT}$-symmetric structure with $n_i > 0$. In addition, $\mathcal{PT}$-symmetry breaking and protection occur at band degeneracies. Detailed views and discussion of these points of interest are provided in the following.

The complex frequency dispersion diagram in Figs. 5(b) and 5(c) has several interesting features. We begin by making a few general observations; further details will be given later for specific points of interest. Along the high-symmetry directions Γ-X and Γ-M, the frequency bands are mostly real. These regions correspond to the $\mathcal{PT}$-symmetric phase. For some bands near the X and M points on the Γ side, thresholdless

spontaneous $\mathcal{PT}$-symmetry breaking can be observed. This is similar to the 1D periodic case in which band merging is exhibited at exceptional points near the Brillouin zone boundary. We note also that as the frequency bands enter the broken-$\mathcal{PT}$-symmetry region at the X point, they remain in the broken-symmetry phase as the in-plane wave vector is swept along the Brillouin zone boundary from the X point to the M point. It is worth mentioning that this $\mathcal{PT}$-symmetry breaking is likely not due to propagation along the low-symmetry directions between the X and M points, but rather results from the general observation that the broken-$\mathcal{PT}$-symmetry phase tends to occur at the Brillouin zone boundary. As the in-plane wave vector is swept along the Brillouin zone boundary from the X point to the M point, the wave vector evolves as $\vec{k} = (\hat{x} + \xi\hat{y})\frac{\pi}{\Lambda}$ with $0 \leqslant \xi \leqslant 1$. As long as the x component of the wave vector is at its maximum value $\frac{\pi}{\Lambda}$, the mode remains in the broken-$\mathcal{PT}$-symmetry phase even as the y component of the wave vector is increased from zero. Alternatively, for a point in the interior of the Brillouin zone [for example, at $\vec{k} = \frac{1}{2}(\hat{x} + \hat{y})\frac{\pi}{\Lambda}$], the eigenfrequencies are mostly real, indicating that the modes remain in the $\mathcal{PT}$-symmetry phase. The conclusion is that the universally broken $\mathcal{PT}$ symmetry seen in the direction of X-M results from general spontaneous $\mathcal{PT}$-symmetry breaking at the Brillouin zone boundary instead of from propagation along a low-symmetry direction in the PC.

We also note that while all bands exhibit $\mathcal{PT}$-symmetry breaking near the X point, some bands do not exhibit symmetry breaking at the M point [bands 1, 2, and 6 (6 not shown at the M point)]. In the following we will provide a field symmetry argument to explain why the $\mathcal{PT}$ symmetry is protected for these modes. Finally, we note that $\mathcal{PT}$-symmetry breaking can be seen at band crossings that occur at k points away from the Brillouin zone boundary. Such midzone band crossings make the 2D band structure distinct from the 1D case. Details of these midzone crossings will be explored in more detail below.

A. Thresholdless $\mathcal{PT}$-symmetry breaking similar to 1D periodic structures (points A and H)

Figure 6 shows a detailed view of the point labeled A in Fig. 5(b). The $\mathcal{PT}$-symmetry breaking at this point is similar in nature to the 1D periodic structure. At the exceptional point the real frequency values merge and the imaginary parts for the two bands are conjugate to each other. The spatial field distributions of the modes at the X point are shown. In particular, the quantity $|H_z(x,y)|$ is displayed. Recalling that the modes of periodic structures are Bloch modes, we note that the field of a mode associated with the qth band at wave vector $\vec{k}$, $H_z(x,y) = u^q_{\vec{k}}(x,y)\exp(-j\vec{k}\cdot\vec{\rho})$, where $\vec{\rho} = \hat{x}x + \hat{y}y$ and $u^q_{\vec{k}}(x,y)$ has the same periodicity as the lattice. Therefore, $|H_z(x,y)| = |u^q_{\vec{k}}(x,y)|$ is the quantity visualized in Fig. 6 and in the spatial field distributions that follow in this work.

As was the case in the 1D structure, there is a gain mode in which the field preferentially overlaps the n_1 rods and a loss mode in which the field preferentially overlaps the n_2 rods. These two modes are shown in Fig. 6. As in the 1D case, the fields for the two modes exhibit the same spatial behavior aside
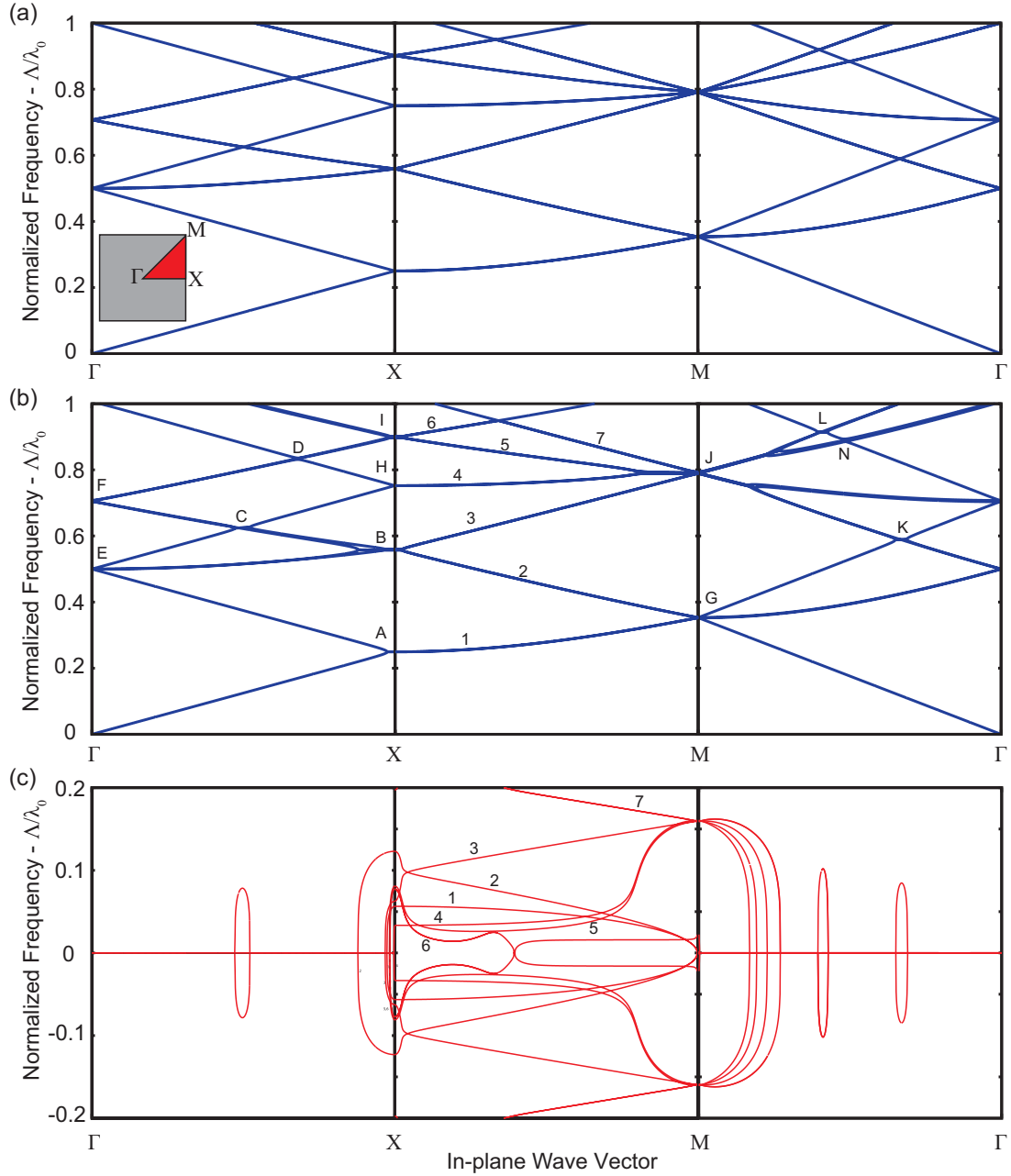
FIG. 5. (a) Photonic band structure for a square lattice with $n_1 = n_2 = n_r = 2.0$, $n_i = 0$. In this case the square lattice is infinitesimal and the light line in the medium is folded into the first Brillouin zone as if there were a finite square lattice perturbation but without any other modification. The inset depicts the first Brillouin zone for the square lattice. High-symmetry points are labeled. The red triangle depicts the region traced by the wave vectors in this work. (b) Photonic band structure for the square lattice shown in Fig. 1 with $n_1 = 2.0 + i0.25$ and $n_2 = 2.0 - i0.25$. The real part of the eigenfrequencies is shown. The letters label points of interest. (c) Same band structure as (b) but the imaginary part of the eigenfrequencies is shown. The numbering between X and M shows the correspondence between the real and imaginary parts of the eigenfrequencies.

from a shift of $\Lambda/2$ along the x direction. We note also that both modes possess the same symmetry along the y direction. In this case, both modes have fields that are uniform along y and therefore have even parity. If σ_y is the parity operator for reflection about the x axis, then $\sigma_y u_{\vec{k}}^{1,2}(x,y) = u_{\vec{k}}^{1,2}(x,-y) = u_{\vec{k}}^{1,2}(x,y)$, where the first two bands are labeled $q = 1,2$ and $\vec{k} = \hat{x}\frac{\pi}{\Lambda}$. We will see that the parity of the mode fields along the direction orthogonal to the propagation direction plays an

important role in $\mathcal{PT}$-symmetry breaking. We note also that point H is of the same general class as point A.

B. Degenerate bands and $\mathcal{PT}$-symmetry breaking at points of fourfold degeneracy (points B and I)

Figure 7 shows a detailed view of the point labeled B in Fig. 5(b). In constructing the folded band diagram in Fig. 5(a) we note that the bands crossing at the X point near the
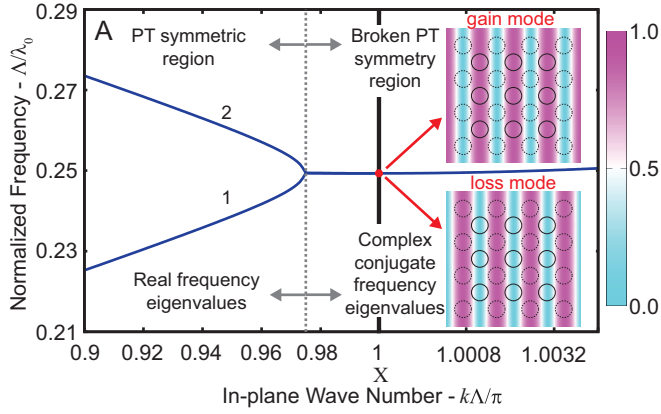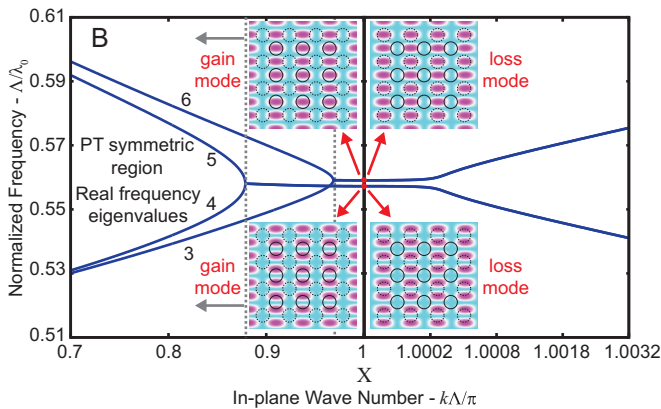
FIG. 6. Detailed view of point A in Fig. 5(b). The numbering scheme here applies to the Γ-X region and is separate from the numbering in Fig. 5(b), which applies to the X-M region. The field profiles for the two modes at the X point are shown. Solid circles correspond to the gain rods n_1 and dashed circles correspond to the absorbing rods n_2.

frequency $\Lambda/\lambda_0 = 0.56$ are each twofold degenerate due to the presence of two equivalent $X^{(2)}$ points [39]. In the presence of the periodic perturbation, the degeneracy is lifted and two distinct but closely spaced bands can be seen. As the bands approach the X point, $\mathcal{PT}$ symmetry is broken and bands merge pairwise to form gain modes and loss modes. The spatial field profiles of all modes are shown in Fig. 7. The fields with preferential overlap of the gain rods (gain modes) and with preferential overlap of the absorbing rods (loss modes) can be seen. The gain and loss modes exhibit half a spatial oscillation per lattice period along the x direction and are distinguished by a $\Lambda/2$ spatial shift also along the x direction, which is similar to modes $q = 1,2$ shown in Fig. 6. However, the field behavior along the y direction is decidedly higher order in nature.

While four bands approach the frequency $\Lambda/\lambda_0 = 0.56$ at the X point, the bands merge pairwise when the $\mathcal{PT}$ symmetry

is broken. Apparently, it is the transverse symmetry that determines which bands merge to form complex-conjugate frequency pairs. The 2D strongly varying refractive index of these structures makes employing the full apparatus of coupled-mode theory beyond the present scope. However, we note qualitatively that the band merging process can be interpreted as the formation of two supermodes where the gain and loss modes are linear superpositions of the nominally $\mathcal{PT}$-symmetric modes of the system. A key quantity in this interpretation is the coupling coefficient between modes in the two bands (here bands 4 and 5). If $E_4(x,y)$ and $E_5(x,y)$ represent components (x or y) of the electric field in bands 4 and 5, respectively, of a nominal $\mathcal{PT}$-symmetric structure with low gain and loss, then the coupling coefficient is of the form

$$\kappa \propto \int_{-\infty}^{\infty} \left[\epsilon^2(x,y) - \epsilon_{\text{nom}}^2(x,y) \right] E_4(x,y)E_5(x,y)dy, \quad (15)$$

where $\epsilon(x,y)$ represents the dielectric of the $\mathcal{PT}$-symmetric structure shown in Fig. 1 and $\epsilon_{\text{nom}}(x,y)$ is the dielectric of a $\mathcal{PT}$-symmetric structure with nominally low (even infinitesimal) gain and loss. Essentially the modes of $\epsilon_{\text{nom}}(x,y)$ possess the requisite symmetry of the lattice but with barely perceptible $\mathcal{PT}$-symmetry breaking (there will be some since the $\mathcal{PT}$-symmetry breaking is thresholdless).

Because $\epsilon^2(x,y) - \epsilon_{\text{nom}}^2$ is even in y (using the origin defined in Fig. 1), $E_4(x,y)$ and $E_5(y)$ must have the same parity in the y direction to obtain nonzero coupling. The slightly-lower-frequency pair shown in Fig. 7 possesses odd parity along the y direction $\sigma_y u_{\vec{k}}^{4,5}(x,y) = u_{\vec{k}}^{4,5}(x,-y) = -u_{\vec{k}}^{4,5}(x,y)$. The odd parity is not immediately apparent in a plot of magnitude, but a plot of the real part of $H_z(x,y)$ (not shown) confirms this conclusion. We point out that the modes of bands 4 and 5 possess the same odd parity along the y direction at k values in the $\mathcal{PT}$-symmetric region (to the left of the exceptional point in Fig. 7), confirming that the odd-y-parity supermodes in the broken-$\mathcal{PT}$-symmetry region can be interpreted as superpositions of modes of the nominally $\mathcal{PT}$-symmetric structure.

The slightly-higher-frequency pair shown in Fig. 7 possesses even symmetry along the y direction $\sigma_y u_{\vec{k}}^{3,6}(x,y) = u_{\vec{k}}^{3,6}(x,-y) = u_{\vec{k}}^{3,6}(x,y)$. From this discussion we conclude that it is the parity of the fields in the direction transverse to the propagation direction that determines whether modes associated with band crossings merge to form complex-conjugate pairs. We note also that this same analysis may be applied to point I in Fig. 5(b).

C. $\mathcal{PT}$-symmetry breaking at band crossings away from the Brillouin zone boundary (points C, K, and L)

Figure 8 shows a detailed view of the point labeled C in Fig. 5(b). The presence of an exceptional point away from the Brillouin zone boundary is a phenomenon that can only be seen in the band diagrams of structures possessing periodicity in more than one dimension. Because they have more directional degrees of freedom, the bands of 2D periodic structures
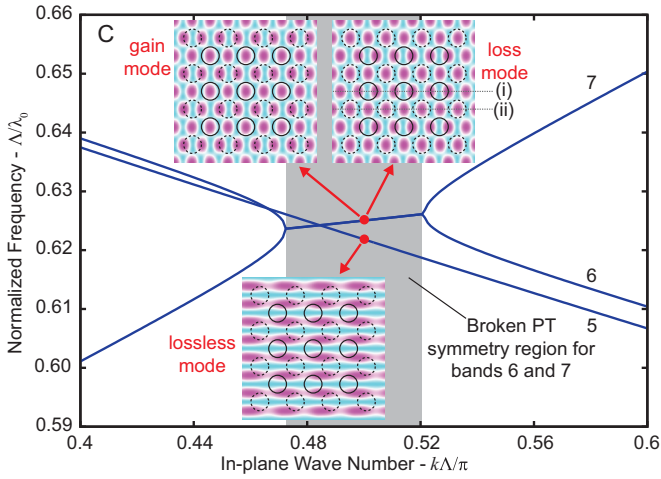

FIG. 7. Detailed view of point B in Fig. 5(b). The numbering scheme here applies to the Γ-X region and is separate from the numbering in Fig. 5(b), which applies to the X-M region. The field profiles for the four modes at the X point are shown. Solid circles correspond to the gain rods n_1 and dashed circles correspond to the absorbing rods n_2. The color scale is the same as in Fig. 6.

FIG. 8. Detailed view of point C in Fig. 5(b). The numbering scheme here applies to the Γ-X region and is separate from the numbering in Fig. 5(b), which applies to the X-M region. The field profiles for the three bands are shown. Solid circles correspond to the gain rods n_1 and dashed circles correspond to the absorbing rods n_2. The color scale is the same as in Fig. 6.

FIG. 9. Detailed view of point D in Fig. 5(b). The numbering scheme here applies to the Γ-X region and is separate from the numbering in Fig. 5(b), which applies to the X-M region. The field profiles for the three bands are shown. Solid circles correspond to the gain rods n_1 and dashed circles correspond to the absorbing rods n_2. The color scale is the same as in Fig. 6.

D. Protected $\mathcal{PT}$ symmetry at band crossings away from the Brillouin zone boundary (points D and N)

Figure 9 shows a detailed view of the point labeled D in Fig. 5(b). In the band diagram for vanishing square lattice perturbation in Fig. 5(a), the point corresponding to the point D in Fig. 5(b) consists of a crossing of a nondegenerate band (connecting the X point at a frequency of 0.75 to the Γ point at a frequency near 1.0) and a doubly degenerate band (connecting the Γ point at a frequency of 0.7 to the X point at a frequency near 0.9). The surprising observation about point D is that $\mathcal{PT}$ symmetry is not broken. At first glance, it contains the same properties as point C where three bands cross and $\mathcal{PT}$ symmetry is broken as the nondegenerate band merges with one of the doubly degenerate bands. At the D point, however, the nondegenerate band (band 8 in Fig. 9) anticrosses one of the doubly degenerate bands (band 9 in Fig. 9) while band 10 passes through the interaction region unaffected. Looking at the spatial field distributions for the different bands, one concludes that band 10 is not expected to mix with these bands to form broken-$\mathcal{PT}$-symmetry supermodes because of its odd parity along y.

To understand why bands 8 and 9 are *protected* from $\mathcal{PT}$-symmetry breaking at the D point band crossing, we take a closer look at the spatial field profiles. For $\mathcal{PT}$-symmetric modes in general, the spatial field distribution overlaps the gain and absorbing regions equally, so the positive and negative contributions to the complex frequency are equal in magnitude and cancel out. When $\mathcal{PT}$ symmetry is broken, the field is preferentially localized in either the gain or absorbing regions. However, when this occurs, the basic symmetry and spatial frequency of the field are maintained and the preferential localization is accomplished by a relative spatial shift between the gain and absorbing modal field distributions. Looking at exceptional points A, B, and C, one sees that the gain and loss modal field distributions differ by a $\Lambda/2$ spatial shift along the x direction. In these cases, when the field is shifted by $\Lambda/2$, the preferential overlap with the gain rods is changed to preferential overlap with the loss rods (and vice versa).

cross not only at high-symmetry points at the Brillouin zone boundaries but also at other arbitrary low-symmetry points. As in the case of the fourfold degeneracy at point B, only modes with nonorthogonal transverse spatial symmetry merge at band crossings. In the band diagram for vanishing square lattice perturbation in Fig. 5(a), the point corresponding to the C point in Fig. 5(b) is threefold degenerate. It consists of a crossing between a nondegenerate band connecting the Γ point at a frequency of 0.5 to the X point at a frequency of 0.75 and the doubly degenerate band rising from the B point labeled in Fig. 5(b).

The detailed view afforded by Fig. 8 shows that the exceptional point behavior is associated with merging of the nondegenerate band connecting the Γ point at a frequency of 0.5 to the X point at a frequency of 0.75 and the higher of the closely spaced bands emerging from point B. Inspection of the associated spatial field distributions shows that the fields associated with the merged bands both possess even symmetry along the y direction. The shaded region in Fig. 8 indicates the broken-$\mathcal{PT}$-symmetry region, but it should be noted that it is only the merged bands that exhibit the broken symmetry. Band 5 as labeled in Fig. 7 passes through the broken-symmetry region, but its $\mathcal{PT}$ symmetry is maintained and its frequency remains real. That the $\mathcal{PT}$ symmetry of band 5 is protected is consistent with its odd parity along the y direction, which makes it orthogonal to modes 6 and 7.

Another interesting feature of the spatial field distribution is the shift in the fields when observed along the lines labeled (i) and (ii) in the inset of Fig. 8. There is a $\pi/2$ shift of the phase between the fields along (i) and (ii), so field peaks along (i) are vertically aligned with field nulls along (ii) (and vice versa). This shift facilitates the different preferential field overlap with the gain and loss rods for the gain and loss modes, respectively.
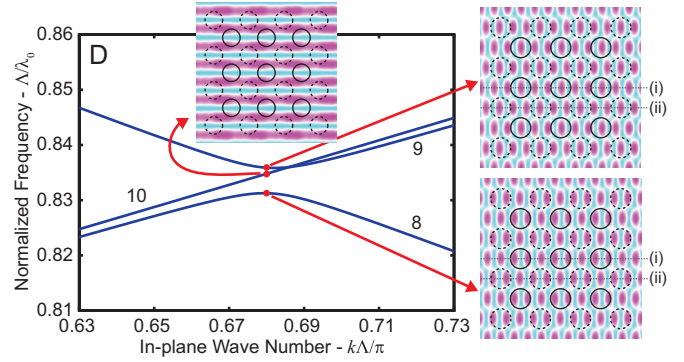
Looking at the spatial field distributions associated with bands 8 and 9 in Fig. 9, one sees that the basic symmetry and spatial frequency of the fields are such that the field overlap with the gain rods and loss rods will always be equal for *any* spatial shift along the x direction.

To investigate this behavior a bit further, consider the field behavior along the dotted lines labeled (i) and (ii) in Fig. 9. Let a simple approximate representation of the field behavior along dotted line (i) be $|u(x,y_i)|^2 \sim \cos^2(\frac{2\pi}{\lambda_x}x)$, where λ_x is the period of the spatial oscillation along x. Counting peaks and nulls in Fig. 9 shows that $\lambda_x = \frac{2}{3}\Lambda$, which results in $|u(x,y_i)|^2 \sim \cos^2(\frac{3\pi}{\Lambda}x)$. As was the case for point C, the phases of the fields along (i) and (ii) are shifted by $\pi/2$, which results in a spatial shift of $\Lambda/6$ or $|u(x,y_{ii})|^2 \approx |u(x-\frac{\Lambda}{6},y_i)|^2 \sim \cos^2[\frac{3\pi}{\Lambda}(x-\frac{\Lambda}{6})] = \cos^2(\frac{3\pi}{\Lambda}x - \frac{\pi}{2})$. As discussed in the previous paragraph, in the broken-$\mathcal{PT}$-symmetry region when the field is shifted by $\Lambda/2$ it should swap the preferential spatial overlap of the gain and loss rods. However, in the present case such a shift applied to the field along dotted line (i) results in $|u(x-\frac{\Lambda}{2},y_i)|^2 \sim \cos^2[\frac{3\pi}{\Lambda}(x-\frac{\Lambda}{2})] = \cos^2(\frac{3\pi}{\Lambda}x - \frac{3\pi}{2}) = \cos^2(\frac{3\pi}{\Lambda}x - \frac{\pi}{2})$. In a broken-$\mathcal{PT}$-symmetry scenario such a shift would produce the corresponding field distribution along dotted line (ii) but for the *conjugate* mode. In the present case the shift produced the field distribution along dotted line (ii) for the *same* mode.

This discussion has not concerned itself with a global phase reference along the x direction; the reason is that the results apply regardless of the chosen phase reference. For example, the fields for bands 8 and 9 in Fig. 9 have a relative phase shift along x of $\Lambda/6$ but both exhibit the property that the fields overlap the gain and loss rods equally. Finally, we point out the special characteristics of point D that facilitate protected $\mathcal{PT}$ symmetry. For spatial fields that possess a $\pi/2$ phase shift between the fields centered on the gain rods [along line (i)] and loss rods [along line (ii)] (as is the case for the C and D points), if a spatial shift of $\Lambda/2$ applied to the field along (i) results in a phase shift of $\pi/2 + m\pi$, where m is an integer, then we expect $\mathcal{PT}$ symmetry to be protected. More concisely, $\mathcal{PT}$ symmetry is protected for modes whose wavelength along the x direction obeys $\Lambda/\lambda_x = m + 1/2$. For point D, $\Lambda/(2/3)\Lambda = 3/2 = 1 + 1/2$; therefore, $\mathcal{PT}$ symmetry is protected. For point C, $\lambda_x = \Lambda$ and $\Lambda/\lambda_x = 1$; therefore, $\mathcal{PT}$ symmetry is expected to be broken. We note also that for spatial fields that do not possess a $\pi/2$ phase shift between the fields centered on the gain rods and loss rods (as in the case for the A and B points), the condition for protected $\mathcal{PT}$ symmetry is $\Lambda/\lambda_x = m$. For points A and B, $\lambda_x = 2\Lambda$ and $\Lambda/\lambda_x = 1/2$; therefore, $\mathcal{PT}$ symmetry is expected to be broken.

E. Behavior at the Γ point ($k = 0$): $\mathcal{PT}$ symmetry and photonic band gaps similar to 1D periodic structures

Figure 10 shows detailed views of the points labeled E and F in Fig. 5(b). In Sec. II it was shown analytically that $\mathcal{PT}$-symmetry breaking was not expected at $k = 0$ in 1D periodic $\mathcal{PT}$-symmetric structures. Instead they had photonic band gaps at this point. For the 2D periodic $\mathcal{PT}$-symmetric structures, similar behavior is seen. The Γ point (which corresponds to $k = 0$) is a high-symmetry point, so
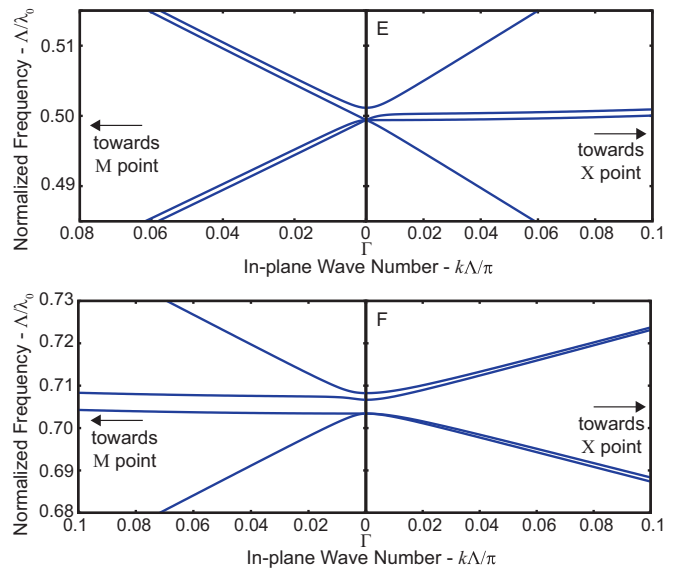

FIG. 10. Detailed view of points E and F in Fig. 5(b). As in the 1D periodic $\mathcal{PT}$-symmetric structure, $\mathcal{PT}$ symmetry is expected to remain unbroken at $k = 0$.

bands either become degenerate there or anticross and form frequency band gaps.

F. $\mathcal{PT}$-symmetry breaking due to lattice symmetry (point G)

Figure 11 shows detailed views of the point labeled G in Fig. 5(b). This point exhibits yet another avenue by which spontaneous $\mathcal{PT}$-symmetry breaking may occur. As the M point is approached from the Γ point (from the right in Fig. 11) $\mathcal{PT}$ symmetry is *not* broken. This is in contrast to nearly every other band crossing at the M and X points in Fig. 5(b). However, in this case the M point itself is an exceptional point as the bands merge pairwise at M and their frequencies become complex and conjugate to each other as the X point is approached from M (moving to the left of the M point in Fig. 11). In this case the $\mathcal{PT}$-symmetry breaking is not spontaneous; rather, it is due to the changing symmetry character of the modes at the M point.

To gain further insight into the behavior of point G, we again examine the spatial field profiles. Here we look at the fields on either side of the exceptional point. In the $\mathcal{PT}$-symmetric region (to the right of the M point in Fig. 11), the frequency bands are all nondegenerate. The M point represents propagation through the lattice at a 45° angle between the x and y directions. The fields depicted in insets 2.a and 3.a possess zeroth-order (i.e., uniform) variation along the propagation direction (which is bottom left to top right). One can see that regardless of any global spatial shift along the propagation direction, the fields will always overlap the gain and loss rods equally, which is the condition for maintaining $\mathcal{PT}$ symmetry. Further, the fields 2.a and 3.a are distinguished by their behavior under the parity operation $\sigma_{d'}$ defined in Fig. 1. The field 2.a is even under $\sigma_{d'}$ and the field 3.a is odd. Because these two modes have opposite parity in the direction transverse to the propagation direction, they are excluded from forming broken-$\mathcal{PT}$-symmetry supermodes.
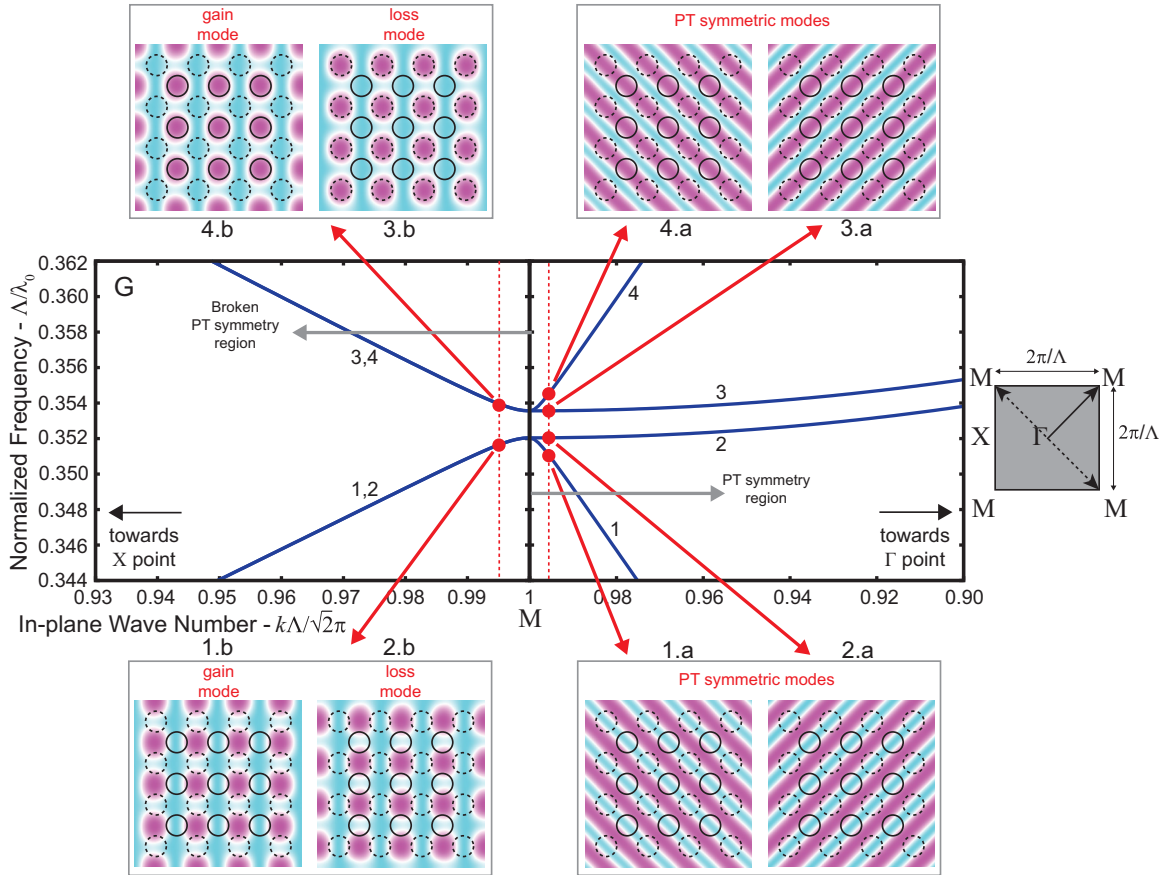
FIG. 11. Detailed view of point G in Fig. 5(b). The numbering scheme here applies to the Γ-M region and is separate from the numbering in Fig. 5(b), which applies to the X-M region. The field profiles for the four bands are shown (1–4) for k values on either side of the M point. Solid circles correspond to the gain rods n_1 and dashed circles correspond to the absorbing rods n_2. The modes labeled a possess $\mathcal{PT}$ symmetry. Modes labeled b are in the broken-$\mathcal{PT}$-symmetry regime. The color scale is the same as in Fig. 6.

The fields labeled 1.a and 4.a can be understood as analogous to the fields at point A (depicted in Fig. 6) but rotated counterclockwise 45° and with a spatial oscillation period adjusted to $\sqrt{2}\Lambda$ from 2Λ. The fields are distinguished by their behavior under the parity operation σ_d defined in Fig. 1. The field in 1.a is even under σ_d and the field in 4.a is odd. Because these two modes have opposite parity in the direction transverse to the propagation direction, they also are excluded from forming broken-$\mathcal{PT}$-symmetry supermodes.

We have provided reasoning for why modes 1.a and 4.a do not merge to break $\mathcal{PT}$ symmetry, and the same holds for modes 2.a and 3.a (orthogonality in the traverse direction). In principle, at point G, modes 1.a and 2.a could also merge as could modes 3.a and 4.a to form broken-$\mathcal{PT}$-symmetry states. In previous sections, we relied on the principle of mode orthogonality in the direction transverse to the propagation direction to predict which bands would merge in the broken-$\mathcal{PT}$-symmetry state. In these cases, the order of the spatial oscillation of the fields was the same along the propagation direction for the merging modes. In the present cases the candidate modes in question have different orders along the propagation direction. Modes 1.a and 4.a are first order along the propagation direction, whereas modes 2.a and 3.a are zeroth order along the propagation direction. This precludes them

from mixing to form spontaneously broken $\mathcal{PT}$-symmetry supermodes. The same principle applies to the mixing of mode 1.a with mode 3.a and mode 2.a with mode 4.a.

At the M point the bottom two and top two bands converge pairwise to degeneracy. The convergence to degeneracy in this case is not inherently related to the $\mathcal{PT}$ symmetry of the structure. Instead it is due to the square symmetry of the lattice. Inspection of fields 1.a and 2.a indicates that field 2.a can be produced by a $\pm 90°$ rotation of field 1.a. Since the fields are calculated a small distance away from the M point, this is true only approximately. At the M point, this statement is precisely true. The same holds for fields 3.a and 4.a. If the wave vector points from the origin to the M point in the Brillouin zone diagram shown to the right in Fig. 11, then a $\pm 90°$ rotation of the wave vector points to another M point. Because this second M point may be reached via a reciprocal lattice vector and it is the same distance from the origin, it is indistinguishable from the initial M point. Therefore, since fields 1.a and 2.a are $\pm 90°$ rotations of each other and propagation at the M point shifted $\pm 90°$ is equivalent, the bands must reach degeneracy at the M point. A similar argument holds for fields 3.a and 4.a. The interesting observation here is that when this degeneracy is reached, $\mathcal{PT}$ symmetry is broken *simultaneously*.
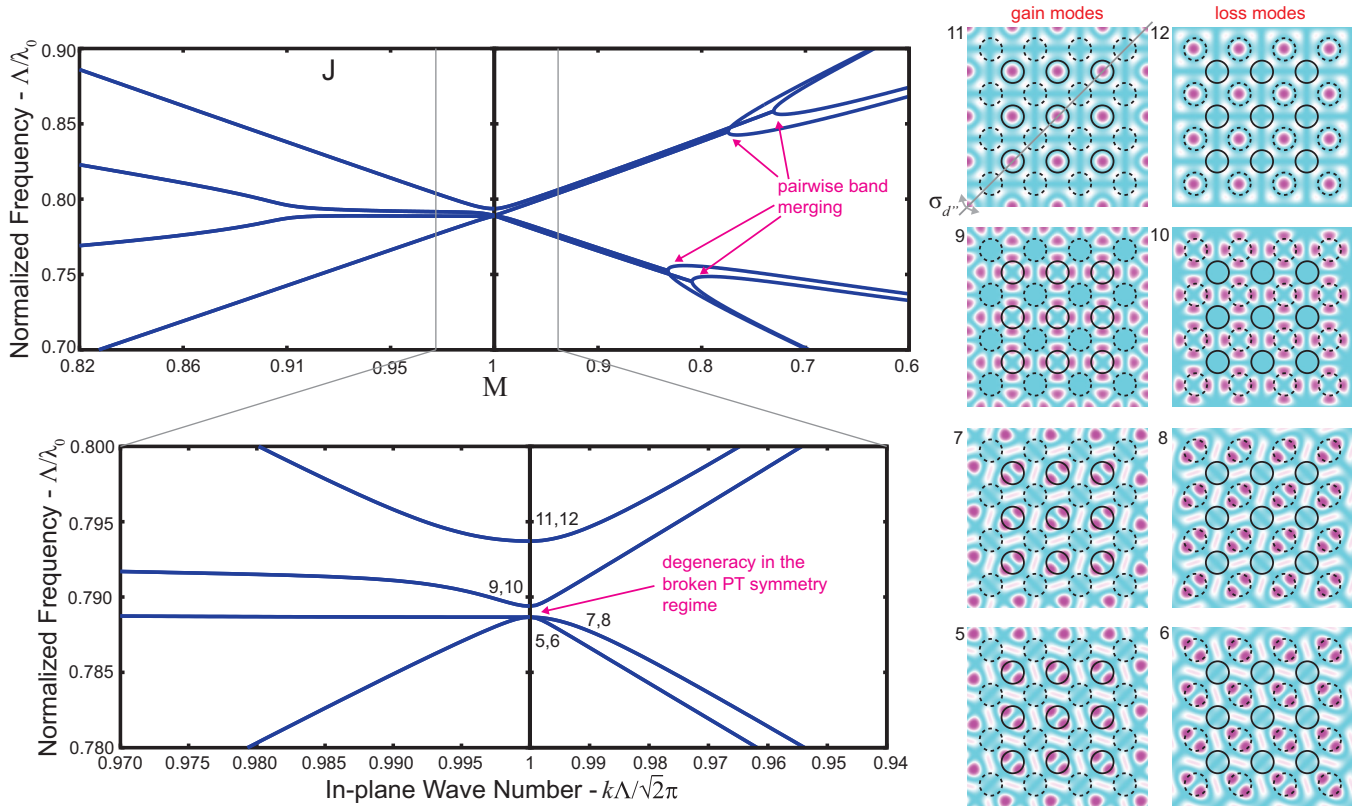
FIG. 12. Two detailed views of point J in Fig. 5(b). The numbering scheme here applies to the Γ-M region and is separate from the numbering in Fig. 5(b), which applies to the X-M region. The top left is the intermediate view showing exceptional points. The bottom left is a further zoom-in showing band degeneracies and anticrossings at the M point. The field profiles for the two twofold degenerate modes and one fourfold degenerate mode are shown on the right. Solid circles correspond to the gain rods n_1 and dashed circles correspond to the absorbing rods n_2. The parity operator $\sigma_{d''}$ is defined to distinguish the character of the eight fields. The color scale is the same as in Fig. 6.

Once the modes enter the broken-$\mathcal{PT}$-symmetry regime (to the left of the M point in Fig. 11), the modes that were nondegenerate to the right of the M point mix to form gain and loss supermodes. In particular, the gain mode $u_{1.b}(x,y)$ can be associated with $u_{1.a}(x,y) + u_{2.a}(x,y)$ and the loss mode $u_{2.b}(x,y)$ can be associated with $u_{1.a}(x,y) - u_{2.a}(x,y)$. Similarly, the loss mode $u_{3.b}(x,y)$ can be associated with $u_{3.a}(x,y) - u_{4.a}(x,y)$ and the gain mode $u_{4.b}(x,y)$ can be associated with $u_{3.a}(x,y) + u_{4.a}(x,y)$.

G. Degeneracy in the broken-$\mathcal{PT}$ phase (point J)

In this subsection we describe one final unique feature of the band structure for 2D periodic structures with $\mathcal{PT}$ symmetry. Figure 12 shows a detailed view of the point labeled J in Fig. 5(b). In the band diagram for vanishing square lattice perturbation in Fig. 5(a), the point corresponding to the J point shows four bands converging to degeneracy. Actually, each of these four bands is twofold degenerate, so the J point in the lattice of infinitesimal perturbation is ultimately eightfold degenerate. The top of Fig. 12 shows a zoomed-in version of the point J. In this view, one sees that the top four bands merge pairwise when $\mathcal{PT}$ symmetry is broken as do the bottom four bands. This is similar to what occurs at the B and I points and is described in Sec. III B above. What makes point J different from points B and I is shown in the second zoomed-in view

shown in the lower left panel of Fig. 12. At the M point, bands labeled 9–12 are pairwise degenerate similar to points B and I. However, the bands labeled 5–8 become fourfold degenerate at the M point while being in the broken-$\mathcal{PT}$-symmetry state.

As in previous discussion, we look to the symmetry of the spatial field profiles of the bands to further understand the behavior at the point J. First we point out that because each band is in the broken-$\mathcal{PT}$-symmetry phase, each band converging to point J is twofold degenerate with one mode having a preferential overlap with the gain rods (gain modes) and the other having a preferential overlap with the absorbing rods (loss modes). In Fig. 12 the fields for the gain modes are on the left (5, 7, 9, and 11) and the fields for the loss modes are on the right (6, 8, 10, and 12). In each case the fields for the gain and loss modes have a relative phase shift of $\sqrt{2}\Lambda/2$ along the propagation direction.

The symmetry of the modes at point J are classified using the parity operator $\sigma_{d''}$ shown in panel 11 in Fig. 12. Modes 11 and 12 are even under $\sigma_{d''}$, whereas modes 9 and 10 are odd under this operation. For this reason band (11,12) and band (9,10) are expected to anticross, which is observed in the calculated band structure. Modes 7 and 8 are even under $\sigma_{d''}$ and modes 5 and 6 are odd. Therefore, due to transverse orthogonality, band (11,12) and band (5,6) anticross and band (9,10) and band (7,8) anticross. To explain the anticrossing of bands (11,12) and (7,8), both of which

have even parity under $\sigma_{d''}$, we point out the higher-order field behavior of mode set (7,8) along the propagation direction. As mentioned in Sec. III F, modes with different spatial frequencies along the propagation direction are precluded from mixing. This argument applies to the anticross of bands (9,10) and (5,6).

So far the behavior described in this section falls into categories described already. The unique aspect of the point J is the degeneracy of modes 5, 6, 7, and 8 at the M point in the broken-$\mathcal{PT}$-symmetry phase. This is the only fourfold degeneracy in the band diagram shown in Fig. 5(b). The distinguishing characteristic of the spatial mode profiles of modes 5–8 is that they are invariant under $180°$ rotations centered at a gain or loss rod, but they are not invariant under $90°$ rotations (modes 9–12 are invariant under $90°$ and $180°$ rotations). However, modes 5 and 7 transform into each other under $90°$ rotations as do modes 6 and 8. At the M point, rotation of the wave vector by $90°$ takes it to another equivalent M point. Therefore, bands with these spatial mode profiles must be degenerate at the M point. A similar argument was given in Sec. III F to explain degeneracy at point G. The

difference here is that the degeneracy is happening within the spontaneously broken-$\mathcal{PT}$-symmetry phase.

IV. CONCLUSION

Parity-time symmetry in two or more spatial dimensions results in rich and varied behavior of the eigenmodes. This work catalogs some of that behavior as it applies to a 2D square lattice with $\mathcal{PT}$ symmetry. These results focus on the mechanisms by which $\mathcal{PT}$ symmetry is or is not broken at band crossings. We find that it depends heavily on the spatial symmetry of the modes. Ultimately, the modes that participate in the formation of broken-$\mathcal{PT}$-symmetry supermodes must be degenerate in frequency and spatially nonorthogonal. These observations will enable understanding of more complicated lattices. For example, a square lattice with a different relative orientation of the loss and gain rods or a $\mathcal{PT}$-symmetric tri-angular lattice would likely result in interesting observations. Another productive next step for this work is analysis of 2D periodic $\mathcal{PT}$-symmetric structures with defects with a view toward photonic crystal waveguides and cavities.

[1] C. M. Bender and S. Boettcher, Real Spectra in Non-Hermitian Hamiltonians Having $\mathcal{PT}$ Symmetry, Phys. Rev. Lett. **80**, 5243 (1998).

[2] C. M. Bender, S. Boettcher, and P. N. Meisinger, $\mathcal{PT}$-symmetric quantum mechanics, J. Math. Phys. **40**, 2201 (1999).

[3] C. M. Bender, D. C. Brody, and H. F. Jones, Complex Extension of Quantum Mechanics, Phys. Rev. Lett. **89**, 270401 (2002).

[4] A. Mostafazadeh, Spectral Singularities of Complex Scattering Potentials and Infinite Reflection and Transmission Coefficients at Real Energies, Phys. Rev. Lett. **102**, 220402 (2009).

[5] A. Mostafazadeh, Resonance phenomenon related to spectral singularities, complex barrier potential, and resonating waveguides, Phys. Rev. A **80**, 032711 (2009).

[6] S. Longhi, $\mathcal{PT}$-symmetric laser absorber, Phys. Rev. A **82**, 031801(R) (2010).

[7] J. Čtyroký, V. Kuzmiak, and Sergey Eyderman, Waveguide structures with antisymmetric gain/loss profile, Opt. Express **18**, 21585 (2010).

[8] H. Benisty, A. Degiron, A. Lupu, A. De Lustrac, S. Chénais, S. Forget, M. Besbes, G. Barbillon, S. Bruyant, S. Blaize, and G. Lérondel, Implementation of $\mathcal{PT}$ symmetric devices using plasmonics: Principle and applications, Opt. Express **19**, 18004 (2011).

[9] L. Ge, Y. D. Chong, and A. D. Stone, Conservation relations and anisotropic transmission resonances in one-dimensional $\mathcal{PT}$-symmetric photonic heterostructures, Phys. Rev. A **85**, 023802 (2012).

[10] W. D. Heiss, Exceptional points of non-Hermitian operators, J. Phys. A: Math. Gen. **37**, 2455 (2004).

[11] R. El-Ganainy, K. G. Makris, D. N. Christodoulides, and Ziad H. Musslimani, Theory of coupled optical $\mathcal{PT}$-symmetric structures, Opt. Lett. **32**, 2632 (2007).

[12] A. Guo, G. J. Salamo, D. Duchesne, R. Morandotti, M. Volatier-Ravat, V. Aimez, G. A. Siviloglou, and D. N. Christodoulides, Observation of $\mathcal{PT}$-Symmetry Breaking in Complex Optical Potentials, Phys. Rev. Lett. **103**, 093902 (2009).

[13] C. E. Rüter, K. G. Makris, R. El-Ganainy, D. N. Christodoulides, M. Segev, and D. Kip, Observation of parity-time symmetry in optics, Nat. Phys. **6**, 192 (2010).

[14] H. Hodaei, M.-A. Miri, M. Heinrich, D. N. Christodoulides, and M. Khajavikhan, Parity-time-symmetric microring lasers, Science **346**, 975 (2014).

[15] L. Feng, Z. J. Wong, R.-M. Ma, Y. Wang, and X. Zhang, Single-mode laser by parity-time symmetry breaking, Science **346**, 972 (2014).

[16] S. Longhi and L. Feng, $\mathcal{PT}$-symmetric microring laser-absorber, Opt. Lett. **39**, 5026 (2014).

[17] L. Chang, X. Jiang, S. Hua, C. Yang, J. Wen, L. Jiang, G. Li, G. Wang, and M. Xiao, Parity-time symmetry and variable optical isolation in active-passive-coupled microresonators, Nat. Photon. **8**, 524 (2014).

[18] B. Peng, Ş. K. Özdemir, F. Lei, F. Monifi, M. Gianfreda, G. L. Long, S. Fan, F. Nori, C. M. Bender, and L. Yang, Parity-time-symmetric whispering-gallery micro cavities, Nat. Phys. **10**, 394 (2014).

[19] S. Phang, A. Vukovic, S. C. Creagh, T. M. Benson, P. D. Sewell, and G. Gradoni, Parity-time symmetric coupled micro resonators with a dispersive gain/loss, Opt. Express **23**, 11493 (2015).

[20] G. Castaldi, S. Savoia, V. Galdi, A. Alù, and N. Engheta, $\mathcal{PT}$ Metamaterials via Complex-Coordinate Transformation Optics, Phys. Rev. Lett. **110**, 173901 (2013).

[21] M. Kang, F. Liu, and J. Li, Effective spontaneous $\mathcal{PT}$-symmetry breaking in hybridized metamaterials, Phys. Rev. A **87**, 053824 (2013).

[22] R. Fleury, D. L. Sounas, and A. Alù, Negative Refraction and Planar Focusing Based on Parity-Time Symmetric Metasurfaces, Phys. Rev. Lett. **113**, 023903 (2014).

[23] Z. H. Musslimani, K. G. Makris, R. El-Ganainy, and D. N. Christodoulides, Optical Solitons in $\mathcal{PT}$ Periodic Potentials, Phys. Rev. Lett. **100**, 030402 (2008).

[24] K. Zhou, Z. Guo, J. Wang, and S. Liu, Defect modes in defective parity-time symmetric periodic complex potentials, Opt. Lett. **35**, 2928 (2010).

[25] Z. Lin, H. Ramezani, T. Eichelkraut, T. Kottos, H. Cao, and D. N. Christodoulides, Unidirectional Invisibility Induced by $\mathcal{PT}$-Symmetric Periodic Structures, Phys. Rev. Lett. **106**, 213901 (2011).

[26] L. Feng, Y.-L. Xu, W. S. Fegadolli, M.-H. Lu, J. E. B. Oliveira, V. R. Almeida, Y.-F. Chen, and A. Scherer, Experimental demonstration of a unidirectional reflectionless parity-time metamaterial at optical frequencies, Nat. Mater. **12**, 108 (2013).

[27] H. Alaeian and J. A. Dionne, Parity-time-symmetric plasmonic metamaterials, Phys. Rev. A **89**, 033829 (2014).

[28] X.-F. Zhu, Y.-G. Peng, and D.-G. Zhao, Anisotropic reflection oscillation in periodic multilayer structures of parity-time symmetry, Opt. Express **22**, 18401 (2014).

[29] M. Kulishov, B. Kress, and H. F. Jones, Novel optical characteristics of a Fabry-Perot resonator with embedded $\mathcal{PT}$-symmetrical grating, Opt. Express **22**, 23164 (2014).

[30] X.-F. Zhu, Defect states and exceptional point splitting in the band gaps of one-dimensional parity-time lattices, Opt. Express **23**, 22274 (2015).

[31] K. G. Makris, R. El-Ganainy, D. N. Christodoulides, and Z. H. Musslimani, Beam Dynamics in $\mathcal{PT}$ Symmetric Optical Lattices, Phys. Rev. Lett. **100**, 103904 (2008).

[32] A. Regensburger, C. Bersch, M.-A. Miri, G. Onishchukov, D. N. Christodoulides, and U. Peschel, Parity-time synthetic photonic lattices, Nature (London) **488**, 167 (2012).

[33] A. Regensburger, M.-A. Miri, C. Bersch, J. Näger, G. Onishchukov, D. N. Christodoulides, and U. Peschel, Observation of Defect States in $\mathcal{PT}$-Symmetric Optical Lattices, Phys. Rev. Lett. **110**, 223902 (2013).

[34] K. S. Agarwal, R. K. Pathak, and Y. N. Joglekar, Exactly solvable-symmetric models in two dimensions, Europhys. Lett. **112**, 31003 (2015).

[35] L. Ge and A. D. Stone, Parity-Time Symmetry Breaking beyond one Dimension: The Role of Degeneracy, Phys. Rev. X **4**, 031011 (2014).

[36] L. Ge, K. G. Makris, D. N. Christodoulides, and L. Feng, Scattering in $\mathcal{PT}$- and $\mathcal{RT}$-symmetric multimode waveguides: Generalized conservation laws and spontaneous symmetry breaking beyond one dimension, Phys. Rev. A **92**, 062135 (2015).

[37] J. Xie, Z. Su, W. Chen, G. Chen, J. Lv, D. Mihalache, and Y. He, Defect solitons in two-dimensional photonic lattices with parity-time symmetry, Opt. Commun. **313**, 139 (2014).

[38] H. Wang, S. Shi, X. Ren, X. Zhu, B. A. Malomed, D. Mihalache, and Y. He, Two-dimensional solitons in triangular photonic lattices with parity-time symmetry, Opt. Commun. **335**, 146 (2015).

[39] K. Sakoda, *Optical Properties of Photonic Crystals* (Springer, Berlin, 2001).

[40] L. A. Coldren and S. W. Corzine, *Diode Lasers and Photonic Integrated Circuits* (Wiley, New York, 1995).

[41] L. Lu, A. Mock, M. Bagheri, E. H. Hwang, J. D. O'Brien, and P. D. Dapkus, Double-heterostructure photonic crystal lasers with reduced threshold pump power and increased slope efficiency obtained by quantum well intermixing, Opt. Express **16**, 17342 (2008).

[42] M. N. Sysak, J. W. Raring, J. S. Barton, M. Dummer, D. J. Blumenthal, and L. J. Coldren, A single regrowth integration platform for photonic circuits incorporating tunable SGDBR lasers and quantum-well EAMs, Photon. Technol. Lett. **18**, 1630 (2006).

[43] A. Yariv and P. Yeh, *Optical Waves in Crystals* (Wiley, Hoboken, 2003).

[44] J. D. Joannopoulos, R. D. Meade, and J. N. Winn, *Photonic Crystals* (Princeton University Press, Princeton, 1995).

[45] M. Plihal, A. Shambrook, A. A. Maradudin, and P. Sheng, Two-dimensional photonic band structures, Opt. Commun. **80**, 199 (1991).

[46] J. Li, L. Zhou, C. T. Chan, and P. Sheng, Photonic Band Gap From a Stack of Positive and Negative Index Materials, Phys. Rev. Lett. **90**, 083901 (2003).

[47] Y. Fan, Z. Wei, H. Li, H. Chen, and C. M. Soukoulis, Photonic band gap of a graphene-embedded quarter-wave stack, Phys. Rev. B **88**, 241403(R) (2013).